eprints@whiterose.ac.uk
https://eprints.whiterose.ac.uk/

What Dictates the Spatial Distribution of Nanoparticles within Calcite?

Yin Ning,[*,†] Lijuan Han,[†] Marcel Douverne,[†] Nicholas J. W. Penfold,[†] Matthew J. Derry,[*,†] Fiona C. Meldrum,[‡] and Steven P. Armes[*,†]

[†] Department of Chemistry, University of Sheffield, Brook Hill, Sheffield, South Yorkshire S3 7HF, UK.

[‡] School of Chemistry, University of Leeds, Woodhouse Lane, Leeds, LS2 9JT, UK.

ABSTRACT: Crystallization is widely used by synthetic chemists as a purification technique because it usually involves the *expulsion* of impurities. In this context, the efficient occlusion of guest nanoparticles within growing host crystals can be regarded as an interesting technical challenge. Indeed, although there are various reports of successful nanoparticle occlusion within inorganic crystals in the literature, robust design rules remain elusive. Herein, we report the synthesis of two pairs of sterically-stabilized diblock copolymer nanoparticles with identical compositions but varying particle size, morphology, stabilizer chain length and stabilizer chain surface density via polymerization-induced self-assembly (PISA). The mean degree of polymerization of the stabilizer chains dictates the spatial distribution of these model anionic nanoparticles within calcite ($CaCO_3$): relatively short stabilizer chains merely result in near-surface occlusion, whereas sufficiently long stabilizer chains are essential to achieve uniform occlusion. This study reconciles the various conflicting literature reports of occluded nanoparticles being either confined to surface layers or uniformly occluded and hence provides important new insights regarding the criteria required for efficient nanoparticle occlusion within inorganic crystals.

INTRODUCTION

The incorporation of guest species into host crystals has gained considerable interest because this bio-inspired strategy provides an attractive route for the preparation of new functional nanocomposites with tailored properties.[1-15] However, the precise design rules for efficient and versatile nanoparticle occlusion within inorganic crystals remain elusive. For example, Lu and co-workers[17] reported that carboxylic acid-functionalized latexes were only incorporated within the surface layer of calcite crystals. Such monodisperse nanoparticles were prepared by co-polymerizing styrene, methyl methacrylate and acrylic acid via miniemulsion polymerization.[18] However, it is difficult to precisely control (or know) the density of carboxylic acid groups at the nanoparticle surface with this synthetic protocol. Subsequently, Kim and co-workers[19] also observed similar surface-confined occlusion when using commercial carboxylate-functionalized polystyrene latexes. More recently, Hanisch *et al.*[20] reported the occlusion of phosphoric acid-functionalized diblock copolymer nanoparticles within calcite. Again, these nanoparticles were preferentially localized within the near-surface layer of calcite crystals. Despite such surface-confined occlusion being observed on multiple occasions for more than a decade, this phenomenon is not properly understood. Indeed, progress in this field to date has mainly relied on empirical trial-and-error experiments. In this context, the elucidation of robust design rules governing efficient na-

noparticle occlusion within crystals would constitute a significant advance.

Reversible addition-fragmentation chain transfer (RAFT) polymerization enables the facile synthesis of well-defined (co)polymers with desired architectures and narrow molecular distributions.[21] Over the past decade or so, RAFT-mediated polymerization-induced self-assembly (PISA) has attracted substantial global attention.[22-27] PISA involves the chain extension of a soluble macromolecular chain transfer agent (macro-CTA) with a suitable monomer to produce a second insoluble block, resulting in the *in situ* formation of sterically-stabilized diblock copolymer nano-objects.[28-30] This robust and versatile methodology offers many advantages. For example, various copolymer morphologies (e.g. spheres, worms or vesicles) can be accessed at high copolymer concentrations (up to 50% w/w) in a wide range of solvents (e.g. water, ethanol, *n*-alkanes etc.).[22-27] Moreover, RAFT-mediated PISA enables the mean degree of polymerization (DP) and chemical functionality of the stabilizer block to be readily adjusted and can also provide some control over the surface chain density in the resulting diblock copolymer nano-objects.[31-34]

Herein we report the PISA synthesis of a range of poly(methacrylic acid)-poly(benzyl methacrylate) (PMAA-PBzMA) diblock copolymer nanoparticles with 0.50 mol% fluorescein *O*-methacrylate being statistically copolymerizing within the poly(benzyl methacrylate)

core-forming block (see **Scheme 1**). These nanoparticles were subsequently transferred to aqueous media by centrifugation (for vesicles) or dialysis (for spheres) against water. We employ electron microscopy, dynamic light scattering (DLS) and small-angle X-ray scattering (SAXS) to characterize these diblock copolymer nanoparticles in terms of their size, morphology and stabilizer chain density. The electrophoretic behavior of these nanoparticles was also investigated as a function of varying solution pH and Ca^{2+} concentration. Scanning electron microscopy (SEM) and confocal laser scanning microscopy (CLSM) are used to visualize the spatial distribution of the occluded nanoparticles within the calcite crystals.
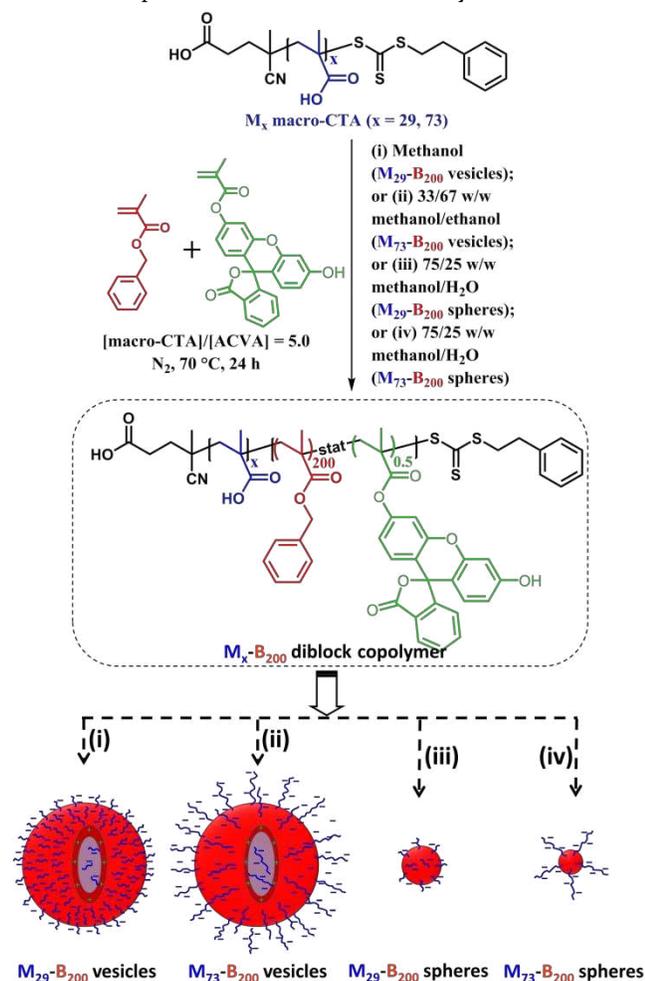
Scheme 1. Synthesis of fluorescein-labeled poly(methacrylic acid)$_x$-poly(benzyl methacrylate)$_{200}$ (M_x-B_{200}) diblock copolymer nanoparticles via RAFT dispersion polymerization of benzyl methacrylate using various solvent compositions; see conditions (i)-(iv). Schematic cartoons show the resulting M_x-B_{200} nano-objects: a mean DP of either 29 or 73 for the poly(methacrylic acid) stabilizer chains can produce either vesicles or spheres depending on the precise solvent composition selected for the PISA synthesis.

The aim of this study is to explore a long-standing question: *which parameters dictate whether nanoparticle occlusion within calcite crystals is uniform, or merely con-*

fined to surface layers? For the sake of brevity, these $PMAA_x$-$PBzMA_y$ diblock copolymers are denoted as M_x-B_y, where x and y indicate the mean DPs of the respective blocks. Moreover, M_x-B_y spheres and M_x-B_y vesicles are indicated as M_x-B_y (S) and M_x-B_y (V), respectively.

RESULTS

Synthesis and Characterization of Diblock Copolymer Nanoparticles. First, two M_x macro-CTAs (where x = 29 or 73) were synthesized via RAFT solution polymerization of methacrylic acid in ethanol (see **Scheme S1** in the Supporting Information). Subsequent chain extension of each macro-CTA with benzyl methacrylate (target DP = 200) via RAFT-mediated PISA led to the formation of either diblock copolymer vesicles [i.e., M_{29}-B_{200} (V) and M_{73}-B_{200} (V)] or spheres [i.e., M_{29}-B_{200} (S) and M_{73}-B_{200} (S)] depending on the precise solvent composition (see **Scheme 1,** and the Supporting Information for detailed synthetic protocols). Specifically, targeting M_{29}-B_{200} in methanol (**Figure 1a**) or M_{73}-B_{200} in a 33/67 w/w methanol/ethanol mixture (**Figure 1b**) gave well-defined, low-polydispersity vesicles (see **Table S1** and SEM images in **Figure S1**). On the other hand, targeting either M_{29}-B_{200} or M_{73}-B_{200} in a 75/25 w/w methanol/water mixture led to the formation of near-monodisperse kinetically-trapped spheres (**Figures 1c** and **1d**). This is attributed to the higher dielectric constant of the latter solvent mixture: this increases electrostatic repulsion between neighboring anionic stabilizer chains and thus prevents vesicle formation.[34-35]
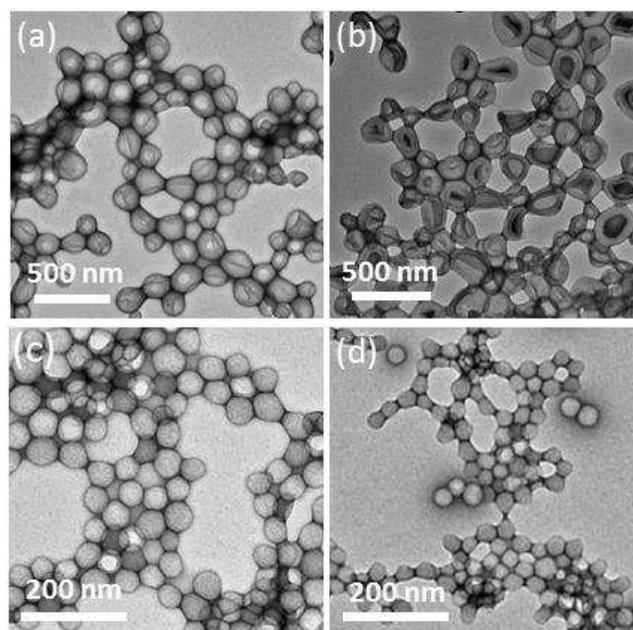
Figure 1. Various anionic poly(methacrylic acid)-poly(benzyl methacrylate) diblock copolymer nanoparticles (either vesicles or spheres) prepared via RAFT-mediated PISA. Representative TEM images recorded for (a) M_{29}-B_{200} vesicles; (b) M_{73}-B_{200} vesicles; (c) M_{29}-B_{200} spheres and (d) M_{73}-B_{200} spheres.

Very high monomer conversions (> 99%) were achieved in all four cases as confirmed by ^{1}H NMR spectroscopy. Gel permeation chromatography (GPC) analyses of exhaustively methylated homopolymers and block copolymers indicated that both M_{29} and M_{73} macro-CTAs gave high blocking efficiencies with minimal macro-CTA contamination (see **Figure S2**). Although each pair of diblock copolymers can self-assemble to form either spherical or vesicular morphologies depending on the precise synthesis conditions, their molecular weight distributions are essentially identical, as indicated by GPC analysis (see **Figure S2**).
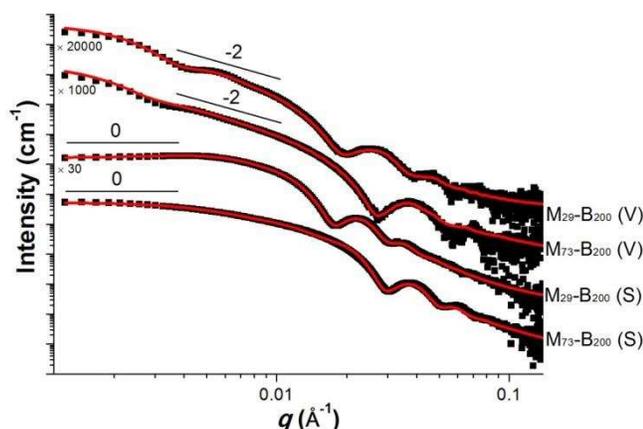
Figure 2. SAXS patterns (black) and corresponding data fits (red) recorded at 20 °C for 1.0% w/w aqueous dispersions of M_{29}-B_{200} vesicles, M_{73}-B_{200} vesicles, M_{29}-B_{200} spheres and M_{73}-B_{200} spheres.

Partially collapsed M_{73}-B_{200} vesicles were observed via transmission electron microscopy (TEM) but this characteristic drying artefact is much less discernible for M_{29}-B_{200} vesicles (see **Figures 1a** and **1b, Figures S1a** and **S1b**). We shall return to this striking difference later (see below). DLS and aqueous electrophoresis analyses of these four nanoparticle dispersions at varying pH and Ca^{2+} ions were performed, as shown in **Figure S3**. In each case, the nanoparticles remained colloidally stable above pH 3 and below $[Ca^{2+}]$ ~ 3.0 mM (see **Figures S3a** and **S3b**). This is important for nanoparticle occlusion experiments (see later), where $CaCO_3$ formation occurs at around pH 9, with a gradual reduction in $[Ca^{2+}]$ during this crystallization process. Aqueous electrophoresis analyses indicated that these nanoparticles became protonated when the pH was lowered to ~5 (see **Figure S3c**). Nanoparticle zeta potentials became much less negative in the presence of Ca^{2+} ions, even at $[Ca^{2+}]$ ~ 0.25 mM (see **Figure S3d**). This observation indicates that Ca^{2+} ions bind to poly(methacrylic acid) chains.[6, 34]

SAXS analysis was performed on these nanoparticles to provide more structural information. This powerful characterization technique enables the nanoparticle morphology, mean diameter (D_{SAXS}), mean aggregation number (N_{agg}), vesicle thickness (T_m) and number of copolymer chains per unit surface area (S_{agg}, or the surface density of stabilizer chains) to be obtained (see Supporting Information for the appropriate mathematical equations).[36] The predominant nanoparticle morphology can be deduced from the gradient at low q, where $I(q) \sim q^{-2}$ indicates vesicles and $I(q) \sim q^0$ is characteristic of non-interacting spheres, as shown in **Figure 2**.[36] Indeed, utilizing previously reported spherical micelle,[37] mixed micelles (i.e., spheres, dimers and trimers),[16] and vesicle[38] models provided satisfactory fits over at least five orders of magnitude of X-ray scattering intensity. As expected, the mean aggregation numbers (or number of copolymer chains per nanoparticle) calculated for the vesicles are significantly larger than that of the corresponding kinetically-trapped spheres. Moreover, the mean vesicle membrane thickness of M_{29}-B_{200} vesicles is significantly thicker than that of M_{73}-B_{200} vesicles (28.4 nm vs. 16.8 nm, see **Table 1**). The four SAXS patterns in **Figure 2** could only be fitted by assuming a solvent volume fraction of zero within the vesicle membrane. Thus the observed difference in mean membrane thickness may indicate differing extents of interdigitation for the membrane-forming poly(benzyl methacrylate) chains.[39-40] This is consistent with TEM observations (see **Figure 1**), which show that the latter vesicles are much more prone to collapse under the ultrahigh vacuum conditions required for TEM studies.

Table 1. Summary of GPC data, DLS diameters and structural parameters derived from SAXS analyses for four types of M_x-B_{200} diblock copolymer nanoparticles.

Copolymer type	GPC[a]		DLS	SAXS				Extent of occlusion
	M_n (g mol^{-1})	M_w/M_n	D_{DLS} (nm)	D_{SAXS} (nm)	T_m (nm)	N_{agg}[b]	S_{agg}[c] (nm^{-2})	(%)[d]
M_{29}-B_{200} (V)	33,800	1.20	195 ± 40	180 ± 39	28.4 ± 3.6	39,140	0.272	3.1 (9.0)
M_{73}-B_{200} (V)	37,200	1.19	205 ± 67	196 ± 67	16.8 ± 1.4	30,900	0.164	9.9 (34.8)
M_{29}-B_{200} (S)	34,000	1.20	63 ± 15	52 ± 5	-	1,200	0.160	1.3 (2.7)
M_{73}-B_{200} (S)	37,700	1.20	43 ± 12	34 ± 3[e]	-	196[e]	0.087[e]	5.6 (11.3)

[a] Poly(methacrylic acid) blocks were fully methylated using trimethylsilyldiazomethane; [b] mean aggregation number; [c] number of copolymer chains per unit surface area; [d] percentage by mass (percentage by volume given in brackets), as determined by thermogravimetric analysis (TGA). [e] These values were calculated based on a single spherical micelle although fitting the SAXS data required the use of a 'mixed micelle' model that includes spheres, dimers and trimers.[16]
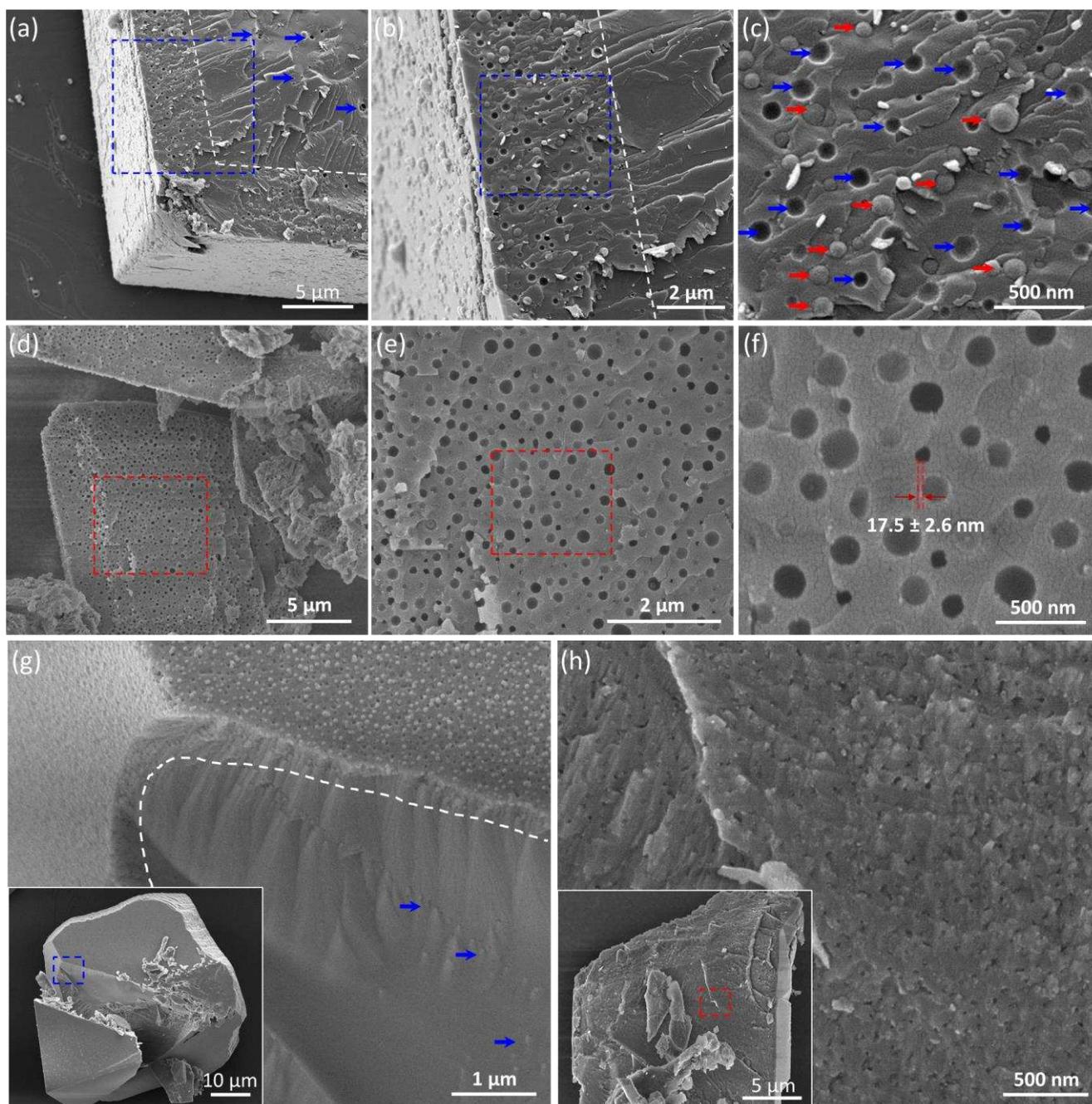
Figure 3. Representative SEM images recorded for randomly-fractured CaCO₃ crystals precipitated in the presence of (a)-(c) 0.1% w/w M_{29}-B_{200} vesicles; (d-f) 0.1% w/w M_{73}-B_{200} vesicles; (g) 0.01% w/w M_{29}-B_{200} spheres and (h) 0.01% w/w M_{73}-B_{200} spheres. (b) and (c) are higher magnification SEM images of the areas indicated by the blue rectangles shown in (a) and (b), respectively. [N.B. Both intact vesicles and empty voids (indicated by red and blue arrows, respectively) were observed because only some of the vesicles remain in each half of the fractured crystal surface]. (e) and (f) are higher magnification SEM images of the areas indicated by the red rectangles shown in (d) and (e), respectively. [N.B. Only voids were observed in this case because the vesicles did not survive the crystal fracture. Moreover, shallow voids contain membrane remnants, as indicated by two dashed lines]. The insets shown in (g) and (h) are the corresponding low magnification SEM images, respectively.

Nanoparticle Occlusion within Calcite Crystals. CaCO₃ crystals were precipitated at $[Ca^{2+}]$ = 1.5 mM in the presence of 0.1% w/w vesicles using the well-known ammonia diffusion method at 20 °C for 24 h.[41] Rhombohedral CaCO₃ crystals with smooth surfaces (and featureless internal structure) were produced in the absence of any additives (see **Figure S4**). In contrast, for CaCO₃ precipitated in the presence of either 0.1% w/w M_{29}-B_{200} (V) or

M_{73}-B_{200} (V) the surface of the crystals was decorated with vesicles (see **Figure S5**). Direct evidence for vesicle occlusion within $CaCO_3$ was obtained by imaging cross-sections of randomly-fractured crystals using SEM, as shown in **Figure 3**. **Figures 3a-3c** indicates that the M_{29}-B_{200} vesicles are preferentially occluded within the near-surface of the crystals, with only a few isolated instances of vesicle occlusion within the crystal interior as indicated by the blue arrows (**Figure 3a**). Such observations are typical of an interesting but perplexing phenomena reported in the literature whereby nanoparticle occlusion within calcite is often surface-confined.[17, 19-20] In striking contrast, spherical voids are densely and uniformly distributed throughout the whole crystal when precipitating $CaCO_3$ in the presence of M_{73}-B_{200} vesicles under identical occlusion conditions (**Figure 3d-3f**). Careful examination of **Figure 3c** and **Figure 3f** reveals some interesting differences. Either empty voids (indicated by blue arrows) or spherical vesicles (indicated by red arrows) are observed in **Figure 3c**, which suggests that the M_{29}-B_{200} vesicles remain intact during crystal fracture. In contrast, **Figure 3f** shows only spherical voids containing remnants of vesicle membranes of ~17.5 nm thickness, which is in good agreement with SAXS analysis of the original vesicles prior to their occlusion ($T_m = 16.8 \pm 1.4$ nm, see **Table 1**). This suggests that the M_{73}-B_{200} vesicles were simultaneously cleaved during fracture of the vesicle/crystal nanocomposites. The differing behavior observed for M_{29}-B_{200} and M_{73}-B_{200} vesicles during fracture of the vesicle/crystal nanocomposites is explained as follows: (i) M_{73}-B_{200} vesicles possess significantly thinner membranes, which makes them inherently weaker and thus more likely to be damaged during crystal fracture; (ii) the same vesicles have longer anionic stabilizer blocks, which penetrate further into the crystal lattice and thus interact more strongly with the $CaCO_3$ matrix.

Since these model nanoparticles were fluorescently-labeled, the spatial distribution of vesicles within the $CaCO_3$ crystals can be studied by CLSM, which enables the crystal cross-section to be visualized without subjecting the crystals to random fracture (see **Figure S6**). CLSM studies indicated that the occluded M_{29}-B_{200} vesicles are mainly surface-confined, as indicated by the fluorescent outline of such crystals (**Figure S6c**). However, the fluorescence intensity on each side of this outline is uneven, which is most likely attributed to the preferential absorption of these vesicles at acute step edges.[42-43] In striking contrast, the M_{73}-B_{200} vesicles are located throughout the $CaCO_3$ crystals since a uniform fluorescent crystal cross-section was observed (**Figure S6h**). Intensity line profiles further support the uniform spatial distribution of such vesicles within $CaCO_3$ (**Figure S6j**). Clearly, these CLSM observations are consistent with the SEM studies.

Similarly, $CaCO_3$ crystals were prepared in the presence of 0.01% w/w M_{29}-B_{200} and M_{73}-B_{200} *spheres* with significantly smaller hydrodynamic diameters of 63 and 43 nm, respectively. Again, M_{29}-B_{200} spheres are located at the crystal surface, with only a few nanoparticles being occluded within the crystal interior, as indicated by the blue

arrows in **Figure 3g**. In contrast, the M_{73}-B_{200} spheres are uniformly occluded (**Figure 3h**). These observations correlate well with those made for the corresponding vesicles. It is perhaps worth emphasizing here that the concentration of spherical nanoparticles used in the latter experiments is an order of magnitude lower than that used for the vesicle occlusion studies. This is because the $CaCO_3$ crystals became significantly elongated along their [001] face when prepared in the presence of 0.1% w/w M_{29}-B_{200} or M_{73}-B_{200} spheres (see **Figure S7**).

Powder X-ray diffraction (XRD) studies indicated that the polymorph of these $CaCO_3$ crystals is exclusively calcite (see **Figure S8**). Raman spectroscopy enables individual crystal polymorphs to be determined, whereby bands at 1088 cm^{-1} (v_1), 712 cm^{-1} (v_4), 281 cm^{-1} and 154 cm^{-1} (lattice modes) are characteristic of calcite (see **Figure S9**).[44-45] In addition, the symmetric breathing vibration (1004 cm^{-1}) and in-plane C-H bending mode (1032 cm^{-1}) of the aromatic rings in the core-forming poly(benzyl methacrylate) block were also detected within these nanocomposite crystals.[46] Interestingly, these latter two band intensities are significantly stronger for M_{73}-B_{200} spheres@calcite and M_{73}-B_{200} vesicles@calcite nanocomposites than those for M_{29}-B_{200} spheres@calcite and M_{29}-B_{200} vesicles@calcite, suggesting higher levels of nanoparticle occlusion are achieved when using the longer anionic stabilizer chain. Indeed, thermogravimetric analysis (TGA, see **Figure S10**) confirmed that the extent of M_{73}-B_{200} nanoparticle occlusion is significantly higher than that of M_{29}-B_{200} nanoparticles. In particular, the extents of occlusion for M_{73}-B_{200} and M_{29}-B_{200} vesicles are 9.9% and 3.1% by mass, which correspond to 34.8% and 9.0% by volume, respectively (see **Table 1**).

DISCUSSION

RAFT-mediated PISA offers a robust platform for the synthesis of various functional nanoparticles because RAFT polymerization is applicable to a wide range of vinyl monomers.[47-53] Although calcite crystals can be precipitated in the presence of *soluble* additives,[54-59] the technical problem of quantifying relatively low levels of incorporation makes analysis of the resulting materials rather challenging. In contrast, guest nanoparticles can be directly imaged within calcite crystals using either SEM, CLSM or atomic force microscopy (AFM).[42, 60-61] This enables the spatial distribution of such nanoparticles within the calcite crystals to be determined (**Figure 3**). Recently, Estroff and co-workers demonstrated three modes of interaction between the nanoparticles and the growing calcite surface via *in situ* AFM studies: (i) nanoparticle attachment followed by detachment, (ii) sticking to and "hovering" over the surface, allowing steps to pass beneath the immobilized nanoparticle, and (iii) incorporation of the nanoparticle by the growing crystals.[61]
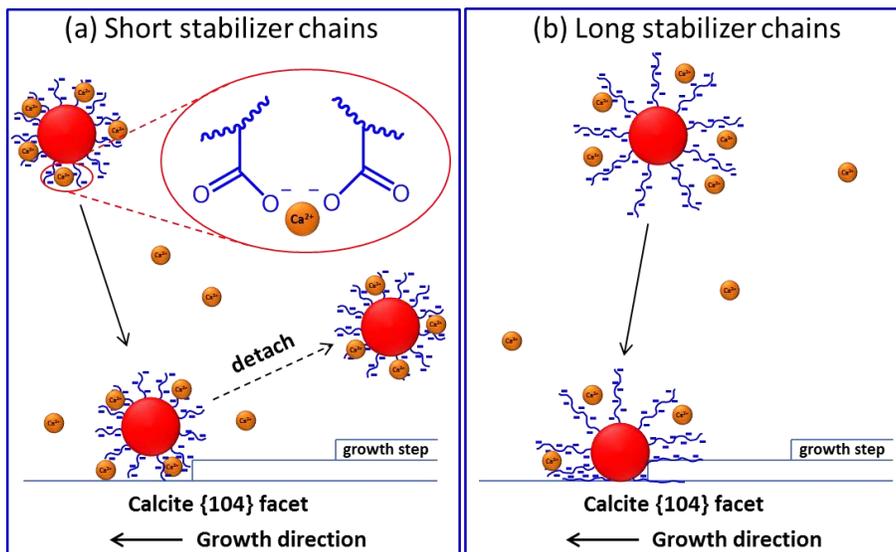
Scheme 2. Schematic cartoons depicting the mechanism that governs the nature and extent of nanoparticle occlusion within calcite. (a) Relatively short poly(methacrylic acid) stabilizer chains (e.g. DP = 29) are extended and adopt fewer possible conformations; they only interact weakly with the growing crystals especially when used at higher [Ca^{2+}], since these divalent cations can act as ionic cross-linkers between the anionic chains. This scenario tends to favor surface-confined occlusion. (b) Relatively long stabilizer chains (DP = 54 or 73) are capable of adopting many more conformations, which facilitates stronger binding to the growing crystal face and hence promotes efficient nanoparticle occlusion.

Which Parameters Dictate Uniform Occlusion? Empirically, it has been shown that anionic surface character is important for driving nanoparticle occlusion within calcite.[61-63] The hydrodynamic diameter of these nanoparticles ranges from 43 nm to 205 nm, as summarized in **Table 1**. Clearly, the spatial distribution of nanoparticles during occlusion is not dictated by particle size, at least within this diameter range. However, smaller nanoparticles do have a more profound influence on the crystal morphology (see **Figure S7**). Given that both M_{73}-B_{200} spheres and M_{73}-B_{200} vesicles can be densely and uniformly occluded, it is evident that the copolymer morphology also plays no significant role. The surface stabilizer density (or S_{agg}) for the four types of nanoparticles studied herein ranges from 0.087 nm^{-2} to 0.272 nm^{-2}, depending on the solvent composition used for the PISA synthesis and the DP of the poly(methacrylic acid) stabilizer block (see **Table 1**). However, S_{agg} does not appear to affect the nature or extent of occlusion, because M_{73}-B_{200} vesicles and M_{29}-B_{200} spheres exhibit comparable surface stabilizer densities (0.164 nm^{-2} vs. 0.160 nm^{-2}, see **Table 1**). In fact, the former nanoparticles are occluded uniformly while only surface-confined occlusion is observed for the latter.

If the influence of nanoparticle size, morphology and surface stabilizer density on occlusion can be excluded, the remaining variable for these model nanoparticles is the poly(methacrylic acid) stabilizer DP. It is perhaps worth emphasizing that these nanoparticles adsorb at the growing crystal faces and are subsequently engulfed by the advancing steps during the occlusion process.[42, 61] Therefore, intimate interaction between the nanoparticles and the growing crystals is the key for efficient occlusion. The relatively short poly(methacrylic acid) stabilizer chains at the surface of M_{29}-B_{200} nanoparticles adopt an extended conformation and hence have fewer degrees of freedom available to interact sufficiently strongly with the growing crystals (see **Scheme 2**). Moreover, the bound divalent Ca^{2+} ions facilitate ionic cross-linking between methacrylic acid residues, which further restricts conformational relaxation. However, nanoparticles possessing longer, more flexible poly(methacrylic acid) chains can adopt many more conformations.[64] This enables stronger interactions between the nanoparticles and the crystal surface, which promotes occlusion. Such long poly(methacrylic acid) chains are more readily intercalated within the crystal lattice by the advancing steps. This explains why M_{73}-B_{200} vesicles are ruptured during random fracture of the calcite crystals, as observed in **Figure 3f**.

One important question remains: how long must the poly(methacrylic acid) stabilizer chain be to ensure uniform nanoparticle occlusion? To address this question, we prepared two further M_x-B_y vesicles with intermediate poly(methacrylic acid) DPs of 36 and 54. SEM studies indicated that the former stabilizer block (DP = 36) did promote a higher level of occlusion (5.0% w/w), but this was not uniform throughout the crystal (see **Figure S11**). Uniform vesicle occlusion within calcite could be achieved by increasing the poly(methacrylic acid) DP up to 54 (see **Figure S12**), although the extent of occlusion achieved for M_{54}-B_{200} vesicles (8.7% w/w) is still lower than that obtained using the M_{73}-B_{200} vesicles (9.9% w/w). These additional experiments provide strong support for our hypothesis that the DP of the anionic stabilizer chains is a critical parameter for determining the extent and uniformity of nanoparticle occlusion within calcite crystals.

Why is Surface-Confined Occlusion Observed for M_{29}-B_{200} Nanoparticles? The surface-confined occlusion observed herein suggests that nanoparticles only begin to become incorporated within the crystals in the latter stages of their growth, when the $[Ca^{2+}]$ is significantly lower than its initial value. Under such conditions, the extent of intra-chain and inter-chain binding by Ca^{2+} cations should be reduced (see **Scheme 2**), so the poly(methacrylic acid) chains gain greater conformational freedom. Therefore, M_{29}-B_{200} nanoparticles can bind more strongly to the step edges, which in turn promotes their occlusion.[34] Consequently, *surface-confined* occlusion of M_{29}-B_{200} nanoparticles occurs, as shown in **Figures 3a** and **3g**. In contrast, the conformational freedom of the longer poly(methacrylic acid) stabilizer chains on the M_{73}-B_{200} nanoparticles is much less affected by the presence of Ca^{2+} ions. Hence *uniform* occlusion can be achieved throughout the whole crystal lattice in this case (see **Figures 3d** and **3h**). It is perhaps also noteworthy that both the mean length of the step edge and the number of kink sites increase as the crystals grow in size,[65] which should also promote M_{29}-B_{200} nanoparticle binding and hence lead to *surface-confined* occlusion.

Although occlusion of M_{29}-B_{200} vesicles and M_{29}-B_{200} spheres within calcite is mainly surface-confined, a few of these nanoparticles were also occluded within the crystal interior, as indicated by the blue arrows shown in **Figures 3a** and **3g**. In principle, this might be attributable to the dispersity of the poly(methacrylic acid) chains (see **Figure S2**). Based on the above discussion, a minor population of nanoparticles containing a higher proportion of longer poly(methacrylic acid) stabilizer chains are more likely to be occluded at an earlier stage of the growth of the calcite crystals.

To further probe the relationship between the mean stabilizer DP of the nanoparticles and their spatial occlusion within calcite, we also examined two phosphoric acid-functionalized nanoparticles with varying stabilizer DPs. Similarly, nanoparticles prepared using a relatively short stabilizer (DP = 32) only exhibited surface-confined occlusion, whereas nanoparticles prepared with a relatively long stabilizer (DP = 51) were uniformly occluded throughout the calcite crystals (see **Figures S13** and **S14**). These additional experiments support our central hypothesis: the anionic stabilizer DP is a critical parameter that dictates the spatial distribution of the nanoparticles within the calcite crystals.

CONCLUSIONS

RAFT-mediated PISA can be used to prepare well-defined anionic diblock copolymer nano-objects of controllable size and morphology with tunable stabilizer chain length and stabilizer surface density. Systematic studies enabled us to establish that the stabilizer chain length dictates the nature of the spatial occlusion of such model nanoparticles within calcite. Our results not only account for the various literature reports of *surface-confined* nanoparticle occlusion, which has been recognized for more than a decade with little or no under-standing, but also provide important new insights regarding the design rules for ensuring efficient *uniform* incorporation of nanoparticles within inorganic crystals. This paves the way for the rational design and synthesis of novel functional nanocomposite crystals. It is well-known that organisms can manipulate organic macromolecules and inorganic materials to produce bespoke biominerals with optimal physical properties. The present study demonstrates that the stabilizer chain length plays an essential role in dictating the spatial distribution of nanoparticles within calcite, which is expected to contribute to a deeper understanding of biomineralization.

ASSOCIATED CONTENT

Supporting Information. Experimental details and characterization methods, Table and Scheme, GPC data, DLS data, aqueous electrophoresis data, CLSM images, Raman spectra, powder XRD data, TGA curves and further SEM images.
This material is available free of charge via the Internet at http://pubs.acs.org.

AUTHOR INFORMATION

Corresponding Author

*Y.Ning@sheffield.ac.uk (Y.N.)
*m.derry@sheffield.ac.uk (M.J.D.)
*s.p.armes@sheffield.ac.uk (S.P.A.)

Notes
The authors declare no competing financial interest.

REFERENCES

1.   Aizenberg, J.; Hanson, J.; Koetzle, T.; Weiner, S.; Addadi, L., *J. Am. Chem. Soc.* **1997,** *119*, 881-886.
2.   Addadi, L.; Joester, D.; Nudelman, F.; Weiner, S., *Chem. Eur. J.* **2006,** *12*, 980-987.
3.   Muñoz-Espí, R.; Qi, Y.; Lieberwirth, I.; Gómez, C. M.; Wegner, G., *Chem. Eur. J.* **2006,** *12*, 118-129.
4.   Wegner, G.; Demir, M. M.; Faatz, M.; Gorna, K.; Munoz-Espi, R.; Guillemet, B.; Gröhn, F., *Macromol. Res.* **2007,** *15*, 95-99.
5.   Metzler, R. A.; Tribello, G. A.; Parrinello, M.; Gilbert, P. U. P. A., *J. Am. Chem. Soc.* **2010,** *132*, 11585-11591.
6.   Kim, Y.-Y.; Ganesan, K.; Yang, P.; Kulak, A. N.; Borukhin, S.; Pechook, S.; Ribeiro, L.; Kroeger, R.; Eichhorn, S. J.; Armes, S. P.; Pokroy, B.; Meldrum, F. C., *Nat. Mater.* **2011,** *10*, 890-896.
7.   Lu, G.; Li, S.; Guo, Z.; Farha, O. K.; Hauser, B. G.; Qi, X.; Wang, Y.; Wang, X.; Han, S.; Liu, X., *Nat. Chem.* **2012,** *4*, 310-316.
8.   Ning, Z.; Gong, X.; Comin, R.; Walters, G.; Fan, F.; Voznyy, O.; Yassitepe, E.; Buin, A.; Hoogland, S.; Sargent, E. H., *Nature* **2015,** *523*, 324.
9.   Liu, Y.; Yuan, W.; Shi, Y.; Chen, X.; Wang, Y.; Chen, H.; Li, H., *Angew. Chem. Int. Ed.* **2014,** *53*, 4127-4131.

10.   Li, H.; Estroff, L. A., *J. Am. Chem. Soc.* **2007,** *129*, 5480-5483.

11.   Li, H.; Xin, H. L.; Muller, D. A.; Estroff, L. A., *Science* **2009,** *326*, 1244-1247.

12.   Li, H.; Estroff, L. A., *Adv. Mater.* **2009,** *21*, 470-473.

13.   Nudelman, F.; Sommerdijk, N. A., *Angew. Chem. Int. Ed.* **2012,** *51*, 6582-6596.

14.   Mann, S., *Oxford University Press: Oxford* **2001**.

15.   Lowenstam, H. A.; Weiner, S., *On biomineralization.* Oxford University Press: New York: 1989.

16.   Lu, C. H.; Qi, L. M.; Cong, H. L.; Wang, X. Y.; Yang, J. H.; Yang, L. L.; Zhang, D. Y.; Ma, J. M.; Cao, W. X., *Chem. Mater.* **2005,** *17*, 5218-5224.

17.   Sakota, K.; Okaya, T., *J. Appl. Polym. Sci.* **1977,** *21*, 1035-1043.

18.   Kim, Y.-Y.; Ribeiro, L.; Maillot, F.; Ward, O.; Eichhorn, S. J.; Meldrum, F. C., *Adv. Mater.* **2010,** *22*, 2082-2086.

19.   Hanisch, A.; Yang, P.; Kulak, A. N.; Fielding, L. A.; Meldrum, F. C.; Armes, S. P., *Macromolecules* **2016,** *49*, 192-204.

20.   Chiefari, J.; Chong, Y.; Ercole, F.; Krstina, J.; Jeffery, J.; Le, T. P.; Mayadunne, R. T.; Meijs, G. F.; Moad, C. L.; Moad, G., *Macromolecules* **1998,** *31*, 5559-5562.

21.   Sun, J.-T.; Hong, C.-Y.; Pan, C.-Y., *Polym. Chem.* **2013,** *4*, 873-881.

22.   Warren, N. J.; Armes, S. P., *J. Am. Chem. Soc.* **2014,** *136*, 10174-10185.

23.   Lowe, A. B., *Polymer* **2016,** *106*, 161-181.

24.   Derry, M. J.; Fielding, L. A.; Armes, S. P., *Prog. Polym. Sci.* **2016,** *52*, 1-18.

25.   Chen, S.-L.; Shi, P.-F.; Zhang, W.-Q., *Chin. J. Polym. Sci.* **2017,** *35*, 455-479.

26.   Wang, X.; Shen, L.; An, Z., *Prog. Polym. Sci.* **2018,** *83*, 1-27.

27.   Wan, W.-M.; Hong, C.-Y.; Pan, C.-Y., *Chem. Commun.* **2009,** 5883-5885.

28.   Blanazs, A.; Madsen, J.; Battaglia, G.; Ryan, A. J.; Armes, S. P., *J. Am. Chem. Soc.* **2011,** *133*, 16581-16587.

29.   Li, Y.; Armes, S. P., *Angew. Chem. Int. Ed.* **2010,** *49*, 4042-4046.

30.   Penfold, N. J.; Ning, Y.; Verstraete, P.; Smets, J.; Armes, S. P., *Chem. Sci.* **2016,** *7*, 6894-6904.

31.   Yao, H.; Ning, Y.; Jesson, C. P.; He, J.; Deng, R.; Tian, W.; Armes, S. P., *ACS Macro Lett.* **2017,** *6*, 1379-1385.

32.   Lesage de la Haye, J.; Zhang, X.; Chaduc, I.; Brunel, F.; Lansalot, M.; D'Agosto, F., *Angew. Chem. Int. Ed.* **2016,** *55*, 3739-3743.

33.   Ning, Y.; Fielding, L. A.; Ratcliffe, L. P. D.; Wang, Y.-W.; Meldrum, F. C.; Armes, S. P., *J. Am. Chem. Soc.* **2016,** *138*, 11734-11742.

34.   Gurnani, P.; Bray, C. P.; Richardson, R. A.; Peltier, R.; Perrier, S., *Macromol. Rapid Commun.* **2018,** 1800314.

35.   Warren, N. J.; Mykhaylyk, O. O.; Mahmood, D.; Ryan, A. J.; Armes, S. P., *J. Am. Chem. Soc.* **2014,** *136*, 1023-1033.

36.   Derry, M. J.; Fielding, L. A.; Warren, N. J.; Mable, C. J.; Smith, A. J.; Mykhaylyk, O. O.; Armes, S. P., *Chem. Sci.* **2016,** *7*, 5078-5090.

37.   Pedersen, J. S., *J. Appl. Cryst.* **2000,** *33*, 637-640.

38.   Bang, J.; Jain, S.; Li, Z.; Lodge, T. P.; Pedersen, J. S.; Kesselman, E.; Talmon, Y., *Macromolecules* **2006,** *39*, 1199-1208.

39.   Rank, A.; Hauschild, S.; Förster, S.; Schubert, R., *Langmuir* **2009,** *25*, 1337-1344.

40.   Battaglia, G.; Ryan, A. J., *J. Am. Chem. Soc.* **2005,** *127*, 8757-8764.

41.   Addadi, L.; Moradian, J.; Shay, E.; Maroudas, N.; Weiner, S., *Proc. Natl. Acad. Sci.* **1987,** *84*, 2732-2736.

42.   Cho, K.-R.; Kim, Y.-Y.; Yang, P.; Cai, W.; Pan, H.; Kulak, A. N.; Lau, J. L.; Kulshreshtha, P.; Armes, S. P.; Meldrum, F. C.; De Yoreo, J. J., *Nat. Commun.* **2016,** *7*, 10187.

43.   Orme, C. A.; Noy, A.; Wierzbicki, A.; McBride, M. T.; Grantham, M.; Teng, H. H.; Dove, P. M.; DeYoreo, J. J., *Nature* **2001,** *411*, 775-779.

44.   Gabrielli, C.; Jaouhari, R.; Joiret, S.; Maurin, G., *J. Raman Spectrosc.* **2000,** *31*, 497-501.

45.   Wehrmeister, U.; Soldati, A. L.; Jacob, D. E.; Haeger, T.; Hofmeister, W., *J. Raman Spectrosc.* **2010,** *41*, 193-201.

46.   Ding, J.; Birss, V. I.; Liu, G., *Macromolecules* **1997,** *30*, 1442-1448.

47.   Ding, Y.; Cai, M.; Cui, Z.; Huang, L.; Wang, L.; Lu, X.; Cai, Y., *Angew. Chem. Int. Ed.* **2018,** *57*, 1053–1056.

48.   Tan, J.; Sun, H.; Yu, M.; Sumerlin, B. S.; Zhang, L., *ACS Macro Lett.* **2015,** *4*, 1249-1253.

49.   Zhang, L.; Lu, Q.; Lv, X.; Shen, L.; Zhang, B.; An, Z., *Macromolecules* **2017,** *50*, 2165-2174.

50.   Huo, M.; Zeng, M.; Li, D.; Liu, L.; Wei, Y.; Yuan, J., *Macromolecules* **2017,** *50*, 8212-8220.

51.   Karagoz, B.; Esser, L.; Duong, H. T.; Basuki, J. S.; Boyer, C.; Davis, T. P., *Polym. Chem.* **2014,** *5*, 350-355.

52.   Zhou, D.; Dong, S.; Kuchel, R. P.; Perrier, S.; Zetterlund, P. B., *Polym. Chem.* **2017,** *8*, 3082-3089.

53.   Deng, R.; Derry, M. J.; Mable, C. J.; Ning, Y.; Armes, S. P., *J. Am. Chem. Soc.* **2017,** *139*, 7616-7623.

54.   Marin, F.; Pokroy, B.; Luquet, G.; Layrolle, P.; De Groot, K., *Biomaterials* **2007,** *28*, 2368-2377.

55.   Paquette, J.; Reeder, R. J., *Geochim. Cosmochim. Acta* **1995,** *59*, 735-749.

56.   Berman, A.; Addadi, L.; Weiner, S., *Nature* **1988,** *331*, 546-548.

57.   Meldrum, F. C.; Cölfen, H., *Chem. Rev.* **2008,** *108*, 4332-4432.

58.   Yu, S. H.; Cölfen, H., *J. Mater. Chem.* **2004,** *14*, 2124-2147.

59.   Guo, X. H.; Yu, S. H.; Cai, G. B., *Angew. Chem. Int. Ed.* **2006,** *45*, 3977-3981.

60.   Ning, Y.; Whitaker, D. J.; Mable, C. J.; Derry, M. J.; Penfold, N. J. W.; Kulak, A. N.; Green, D. C.; Meldrum, F. C.; Armes, S. P., *Chem. Sci.* **2018,** *9*, 8396-8401.

61.   Hendley, C. T.; Fielding, L. A.; Jones, E. R.; Ryan, A. J.; Armes, S. P.; Estroff, L. A., *J. Am. Chem. Soc.* **2018,** *140*, 7936-7945.

62.   Ning, Y.; Fielding, L. A.; Doncom, K. E. B.; Penfold, N. J. W.; Kulak, A. N.; Matsuoka, H.; Armes, S. P., *ACS Macro Lett.* **2016,** *5*, 311-315.

63.   Ning, Y.; Fielding, L. A.; Andrews, T. S.; Growney, D. J.; Armes, S. P., *Nanoscale* **2015,** *7*, 6691-6702.

64.   de Gennes, P. G., *Macromolecules* **1980,** *13*, 1069-1075.

65.   Kim, Y. Y.; Freeman, C. L.; Gong, X.; Levenstein, M. A.; Wang, Y.; Kulak, A.; Anduix-Canto, C.; Lee, P. A.; Li, S.; Chen, L., *Angew. Chem.* **2017,** *129*, 12047-12052.

TOC   What Dictates the Spatial Distribution of Nanoparticles within Calcite?